

Efficient qubit detection using alkali earth metal ions and a double STIRAP process

Ditte Møller,* Jens L. Sørensen, Jakob B. Thomsen, and Michael Drewsen
*QUANTOP - Danish National Research Foundation Center for Quantum Optics,
 Department of Physics and Astronomy, University of Aarhus, DK-8000, Denmark.*
 (Dated: August 21, 2021)

We present a scheme for robust and efficient projection measurement of a qubit consisting of the two magnetic sublevels in the electronic ground state of alkali earth metal ions. The scheme is based on two stimulated Raman adiabatic passages (STIRAP) involving four partially coherent laser fields. We show how the efficiency depends on experimentally relevant parameters: Rabi frequencies, pulse widths, laser linewidths, one- and two-photon detunings, residual laser power, laser polarization and ion motion.

PACS numbers: 03.67.Lx, 32.80.Qk, 39.30.+w

I. INTRODUCTION

Quantum computation is a promising technique for efficient solving of high complexity problems, which are inaccessible by classical algorithms [1]. Currently, efforts are made within many fields of physics in order to explore the possibility of realizing quantum computing. Notable examples are superconducting circuits [2, 3], semiconductors [4], linear optics with single photons [5, 6], cold neutral atoms in cavities [7] and lattices [8, 9, 10] as well as cold, trapped ions [11]. So far, most progress has been made in ion trap systems [12, 13, 14, 15, 16, 17] where quantum gates [12, 13], many qubit entanglement [18, 19] and quantum error correction has been demonstrated [20].

The qubit states most successfully implemented with trapped ions are two hyperfine components of the $^9\text{Be}^+$ ground state [12] and a combination of the metastable $3D_{5/2}$ state and the $4S_{1/2}$ ground state in $^{40}\text{Ca}^+$ [13]. In both cases linear Paul traps are used to confine the ions. In this work we consider the electron spin in the alkali earth metal ion ground state as a qubit. In Fig. 1 the electronic ground state is denoted by $|1\rangle$ and the qubit basis by $|\uparrow\rangle$ and $|\downarrow\rangle$. Single qubit operations as well as gate operations can be performed by driving stimulated Raman transitions between the two qubit states [21], or alternatively using controlled mechanical light forces [22]. Since solely ground states are involved, the qubit decoherence will be limited only by ambient noise fields and ion heating effects, rather than excited state lifetimes. Limitations due to ambient magnetic field noise can be avoided using logical qubits of a decoherence-free subspace [23, 24]. In order to achieve fault tolerant quantum computation the detection error rate must be kept low and different error correction codes estimates allowed error rates between 10^{-5} and 10^{-2} [25, 26]. However, high error rates require a large overhead of qubits to encode the error correction. In this paper we present a scheme for potentially efficient qubit projective measure-

ments via shelving of population of one qubit state in the long lived metastable $D_{5/2}$ state found in the isotopes with no nuclear spin of the alkali earth metal ions Ca^+ , Sr^+ and Ba^+ as well as the transition metal ion Hg^+ .

The qubit shelving is performed via a double Stimulated Raman Adiabatic Passage (STIRAP) process [27, 28], as illustrated in Fig. 1. Initial and final states of the shelving process are denoted $|\downarrow\rangle$ and $|5\rangle$ respectively. After shelving, the atomic population remaining in the $|\uparrow\rangle$ state can be observed directly by resonantly driving the $|1\rangle \rightarrow |2\rangle$ and $|3\rangle \rightarrow |2\rangle$ transitions and monitoring the fluorescence [29]. We use the first STIRAP

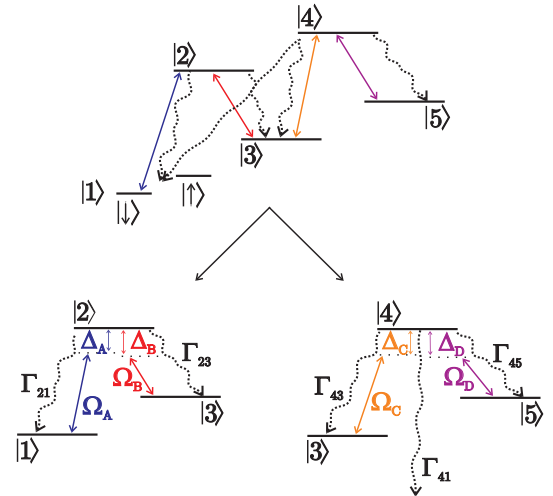


FIG. 1: (Color) Relevant energy levels of isotopes of Ca^+ , Sr^+ , Ba^+ and Hg^+ with no nuclear spin: $|1\rangle = |S_{1/2}\rangle$, $|2\rangle = |P_{1/2}\rangle$, $|3\rangle = |D_{3/2}\rangle$, $|4\rangle = |P_{3/2}\rangle$ and $|5\rangle = |D_{5/2}\rangle$. We consider the qubit encoded in the Zeeman sublevels, $|\uparrow\rangle$ and $|\downarrow\rangle$ of the electronic ground state, $|1\rangle$. The states $|3\rangle$ and $|5\rangle$ are metastable with lifetimes varying from a fraction of a second to many seconds depending on the ion species. The decay of these states is neglected here. Since the scheme consists of two stages of STIRAP, we break down the five level system into two three level Λ systems, each coupled by two optical fields.

*Electronic address: dittem@phys.au.dk

process to transfer the population from $|\downarrow\rangle$ to $|3\rangle$, where we achieve the spin-state selectivity by using circularly right handed polarized light to couple the states $|\downarrow\rangle$ and $|2\rangle$. The second process transfers the population from $|3\rangle$ to the non-fluorescent state, $|5\rangle$. A weak externally applied magnetic field defines the quantization axis and creates a Zeeman splitting of $|\downarrow\rangle$ and $|\uparrow\rangle$ (See Fig. 1).

STIRAP has been shown to be a robust way of adiabatically transferring population from one quantum state to another in a three level lambda-system using two laser pulses in a counterintuitive order [28, 30, 31, 32, 33, 34, 35, 36, 37]. Compared to population transfer via π -pulses or rapid adiabatic passage, STIRAP has the advantage that no strict control of laser amplitude and phase is required to maintain a high efficiency [38]. However, STIRAP does require the pairs of laser pulses involved to be phase coherent relative to each other. In practice, this means that either the lasers must be mutually phase locked or the laser pulses sufficiently short, such that laser decoherence is negligible. The latter method is experimentally attractive because high obtainable Rabi frequencies permit short pulses to be used and hence laser phase locking is circumventable. This approach has previously been used in the experimental realizations of STIRAP [28, 37]. Also note that the two STIRAP stages can be decoupled within the lifetime of intermediate metastable state, $|3\rangle$. Of course decoherence is always at play. Hence, in the numerical calculations below we assume finite laser linewidths and only partially coherent lasers.

The goal of this work is to theoretically investigate the shelving process and identify the parameters of importance to its efficiency. In Sec. II we first make some general remarks on the STIRAP-process. This analytical treatment is valid for any three level Λ system and it serves to develop the criteria for maintaining adiabaticity using Gaussian shaped pulses. We then turn to numerical simulations of the density matrix evolution for the full five level system. Here, we consider the roles of one- and two-photon detunings of the Raman resonances, laser linewidths, laser pulse widths, Rabi frequencies, stray laser light, laser polarizations and ion motion. The results are presented in Sec.'s IV and V. Here we use as an example the $^{40}\text{Ca}^+$ ion, but, apart from different decay rates and wavelengths, our treatment is also valid for Sr^+ , Ba^+ and Hg^+ ions with no nuclear spin. In Sec. VI we present simulations taking all effects into account and finally we conclude in Sec. VII.

II. STIRAP WITH GAUSSIAN PULSES

Let us first consider one STIRAP process involving the three atomic basis states ($|1\rangle, |2\rangle, |3\rangle$). In this section we will neglect spontaneous decay of the $|2\rangle$ state, since this is of no importance to the adiabaticity underlying STIRAP. Two mutually coherent and monochromatic laser fields A (pump field) and B (Stokes field) couples $|1\rangle$ and

$|3\rangle$ to $|2\rangle$ (See Fig. 2(a)). The interaction Hamiltonian for this system in the rotating wave approximation is given by

$$H_I(t) = \frac{\hbar}{2} \begin{pmatrix} 0 & \Omega_A(t) & 0 \\ \Omega_A(t) & 2\Delta_A & \Omega_B(t) \\ 0 & \Omega_B(t) & 2(\Delta_A - \Delta_B) \end{pmatrix} \quad (1)$$

where Δ_A and Δ_B are the detunings of the two applied fields having the real, time dependent Rabi frequencies, $\Omega_A(t)$ and $\Omega_B(t)$ respectively. These parameters are defined as in [28]. On two-photon resonance, $\Delta_A - \Delta_B = 0$, diagonalizing (1) yields the eigenvalues

$$\omega^\pm = \frac{1}{2}(\Delta_A \pm \sqrt{\Delta_A^2 + \Omega_A^2 + \Omega_B^2}) , \quad \omega^d = 0, \quad (2)$$

corresponding to eigenstates

$$\begin{aligned} |+\rangle &= \sin(\alpha) \sin(\beta) |1\rangle + \cos(\beta) |2\rangle - \cos(\alpha) \sin(\beta) |3\rangle, \\ |-\rangle &= \sin(\alpha) \cos(\beta) |1\rangle - \sin(\beta) |2\rangle + \cos(\alpha) \cos(\beta) |3\rangle, \\ |d\rangle &= \cos(\alpha) |1\rangle - \sin(\alpha) |3\rangle, \end{aligned} \quad (3)$$

with $\tan(\alpha) = \frac{\Omega_A(t)}{\Omega_B(t)}$ and $\tan(\beta) = \sqrt{-\frac{\omega^-}{\omega^+}}$. The $|d\rangle$ -state has zero interaction energy and hence it is decoupled from the light. As a result adiabatic following of this state does not populate of the potentially short-lived $|2\rangle$ -state. Now, with all population initially in $|1\rangle$ and only the Stokes field applied, this initial state is $|d\rangle$. Adiabatically decreasing Ω_B while increasing Ω_A corresponds to a variation of $\tan(\alpha)$ from 0 to ∞ . The pulse sequence thus changes the dressed state $|d\rangle$, from $|1\rangle$ to $|3\rangle$.

Since STIRAP requires adiabatic following of atoms while remaining in the $|d\rangle$ -state, we will now consider the criterion for this to happen. We assume essentially Fourier limited optical pulses with a Gaussian time dependence. These give rise to the time varying Rabi frequencies

$$\begin{aligned} \Omega_A(t) &= \Omega_{A,0} \exp \left[-\left(\frac{t - \Delta t/2}{\tau/2} \right)^2 \right], \\ \Omega_B(t) &= \Omega_{B,0} \exp \left[-\left(\frac{t + \Delta t/2}{\tau/2} \right)^2 \right] \end{aligned} \quad (4)$$

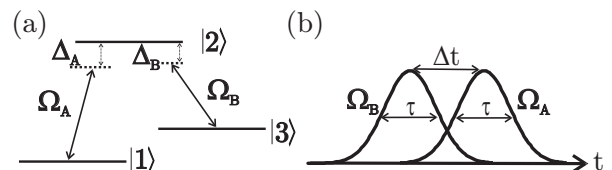


FIG. 2: (a) Three level lambda-system with a pump laser (A) and a Stokes laser (B) applied. The two laser fields have Rabi frequencies Ω_A and Ω_B and they are detuned Δ_A and Δ_B from resonance. (b) STIRAP pulse sequence. Δt is the pulse separation and τ is the full width at $1/e$ height for both pulses.

where the peak Rabi frequencies are $\Omega_{A,0}$ and $\Omega_{B,0}$, Δt is the pulse separation and τ is the full width at $1/e$ height, assumed to be the same for both pulses (See pulse sequence in Fig. 2(b)). We parameterize the problem in terms of the scaled time, $\theta = \sqrt{8}t/\tau$, scaled pulse separation, $\eta = \sqrt{2}\Delta t/\tau$ and Rabi frequency asymmetry $r = \Omega_{A,0}/\Omega_{B,0}$. Hence

$$\begin{aligned}\Omega_A(\theta) &= \Omega_{A,0} \exp \left[-1/2 (\theta - \eta)^2 \right], \\ \Omega_B(\theta) &= \Omega_{B,0} \exp \left[-1/2 (\theta + \eta)^2 \right],\end{aligned}\quad (5)$$

and

$$|d\rangle = -\frac{r^{-1/2}e^{-\eta\theta}|1\rangle - r^{1/2}e^{\eta\theta}|3\rangle}{\sqrt{re^{2\eta\theta} + r^{-1}e^{-2\eta\theta}}}.\quad (6)$$

Adiabaticity requires the rate of change of the wave function to be small compared to the energy separation between the dressed state eigenvalues,

$$\left| \frac{d}{dt}|d\rangle \right| \ll |\omega_{\pm}|.\quad (7)$$

The rate of change of the wave function (6) is parameterized by the Bloch sphere polar angle in the $\{|1\rangle, |3\rangle\}$ basis, which from (3) and (6) is found to be $\alpha = \arctan[r \exp(2\eta\theta)]$. The wave function rate of change is then

$$\frac{d\alpha}{d\theta} = \frac{2\eta}{re^{2\eta\theta} + r^{-1}e^{-2\eta\theta}}.\quad (8)$$

This should be compared to the dimensionless eigenvalue of the energetically closest dressed state, $|- \rangle$. On two-photon resonance and in the limit of large single photon detuning, $\Omega_{A,0}, \Omega_{B,0} \ll |\Delta_A|$, the eigenvalue is given by

$$\lambda_- = \frac{\omega^- \tau}{\sqrt{8}} = -2\Lambda (re^{2\eta\theta} + r^{-1}e^{-2\eta\theta}) \exp[-(\theta^2 + \eta^2)],\quad (9)$$

We can now formulate an adiabaticity criterion, which should be fulfilled at all times during the pulse sequence, where the Rabi frequencies are appreciable. The criterion states that

$$A(\theta, \eta, r) \equiv \frac{|\eta| \exp[\theta^2 + \eta^2]}{(re^{2\eta\theta} + r^{-1}e^{-2\eta\theta})^2} \ll \Lambda,\quad (10)$$

where we identify the parameter relevant for maintaining adiabaticity

$$\Lambda = \frac{\Omega_{A,0}\Omega_{B,0}}{16\sqrt{2}|\Delta_A|}\tau.\quad (11)$$

On inspection Λ is simply proportional to the product of the maximum achievable Raman Rabi frequency and the duration of the pulse sequence. Hence, Eq. (10) simply states that many Raman Rabi cycles should take place during the time span of the STIRAP process, analogous to the result derived in [28].

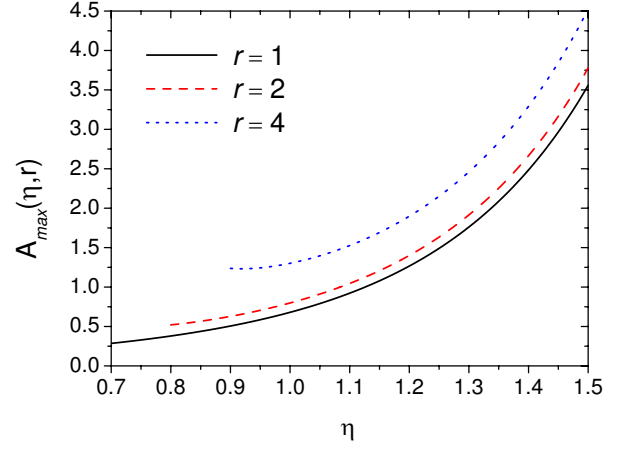


FIG. 3: (Color) Maximum value of the adiabaticity function, $A_{max}(\eta, r) = A(\theta_{max}, \eta, r)$ as function of STIRAP pulse separation, η , for $r = 1$, $r = 2$ and $r = 4$. For $r > 1$ a solution does not exist for smaller η values, hence the truncation of the corresponding curves. The maximum is found by solving Eq. (12).

The timing of the STIRAP sequence is contained in the function $A(\theta, \eta, r)$. For a range of parameters this has a maximum as function of time, $A_{max}(\eta, r) = A(\theta_{max}, \eta, r)$, where θ_{max} solves the equation

$$2 \tanh(2\eta\theta_{max} + \ln r) = \theta_{max}/\eta.\quad (12)$$

For an efficient STIRAP process to occur, given a certain value of r , we obviously want to choose the pulse separation, η , so that A_{max} is small and obeys the inequality (10).

In Fig. 3 we plot A_{max} as function of η for values, where Eq. (12) has a solution. The three curves correspond to $r = \{1, 2, 4\}$ and it should be noted that $A_{max}(\eta, r) = A_{max}(\eta, r^{-1})$. From the graphs we infer that values of Λ in excess of 3-5 should be obtained in order to ensure efficient population transfer. Adiabaticity is favored when the pulse separation is decreasing toward $\eta = 0.7$ and when the Rabi frequencies are balanced, corresponding to r approaching unity. In an experimental situation [37] residual light illuminating the ions before and after the STIRAP pulse sequence can become a severe limitation to the population transfer efficiency. This will be discussed in more detail in Sec. IV E, where one conclusion is that a short duration of the experiment is needed in order to avoid population repumping due to residual light driving a parasitic Raman resonance. Hence, we introduce the time duration of the experiment, Θ , which when inserted in Eq. (6) provide the population transfer efficiency:

$$P_3(\Theta) = [1 + r^{-2} \exp(-4\eta\Theta)]^{-1}.\quad (13)$$

Obviously, (13) shows that the transfer efficiency grows with increasing η , due to the tails of the Gaussian pulses. However, for larger η fulfilling the adiabaticity criteria

(10) becomes difficult and we hence expect to find an optimum value of the pulse separation, η_{opt} , which depends only on r and Λ . With respect to r , $P_3(\Theta)$ grows for high values, while adiabaticity requires values close to unity and therefore one might expect an optimal value of r above 1 with the exact value depending on Λ . To optimize the transfer efficiency with respect to η and r , we solve the optical Bloch equations for the three level Λ system. Details of our derivation of the Bloch equations can be found in the next section.

In order to make our Bloch equation solutions general, we again ignore the decay from the short lived state $|2\rangle$ and we assume perfectly coherent laser fields. The Bloch equations are integrated numerically for one-photon detunings of 4 GHz. These detunings are chosen sufficiently large, so that for Rabi frequencies in the 100 MHz range, the results are independent of the specific values of the detunings. It is checked numerically that increasing the detunings even more has no impact on the solutions. In this limit our results can be considered general and system independent.

For fixed values of r and Λ the population transfer is computed as a function of η , and the optimum value, η_{opt} , corresponding to the maximum population transfer, P_{max} , is found. Examples of such curves can be found in Sec. IV A, where we analyze the sensitivity of the population transfer with respect to fluctuations of η . Fig. 4(a) shows η_{opt} as function of r for $\Lambda = \{1, 3, 10\}$. From the curves it is found that for values of r far from unity, a larger pulse separation is preferable. As mentioned above, this is attributed to the wings of the larger amplitude Gaussian pulse, which must decay ($r < 1$) - or grow ($r > 1$) sufficiently before the pulse sequence is terminated. This is also the reason why η_{opt} grows from about 0.7 for $\Lambda = 1$ to about 1.1 for $\Lambda = 10$. Fig. 4(b) shows the population transfer inefficiency, $1 - P_{max}$, associated with the values of η_{opt} computed in Fig. 4(a). From these curves it is obvious that balanced Rabi frequencies are crucial for an efficient population transfer when the adiabaticity criterion (10) is only marginally fulfilled, as it is the case for $\Lambda = 1$. As Λ grows, we see that higher asymmetries in the Rabi frequencies can be tolerated. This is in accordance with the discussion of Fig. 3. It should be noted that the inclusion of finite laser linewidths tends to make η_{opt} smaller as a result of decoherence mechanisms explained in Sec. IV C. For the remaining simulations in this paper we have sought to use optimum values of η according to the reasoning above.

Although Fig. 4(b) shows that the fidelity of qubit detection in general can be high for $\Lambda = 10$, it should be noted that the difference between a detection error of 10^{-3} and 10^{-5} becomes very important when error correction protocols are considered [1]. Hence, optimizing the fidelity with respect to r , according to Fig. 4(b), could be crucial if the qubit detection scheme should be utilized for scalable quantum computation.

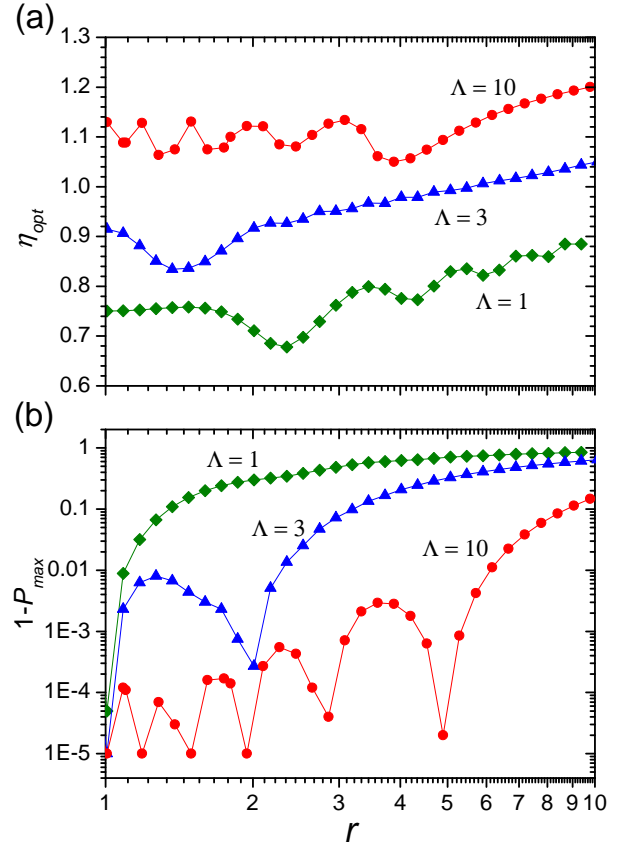


FIG. 4: (Color) (a) Optimum pulse separation, η_{opt} as function of Rabi frequency ratio, $r = \Omega_{A,0}/\Omega_{B,0}$. As indicated, the three curves correspond to different values of Λ , given by $\Lambda = 1$ (\blacklozenge), $\Lambda = 3$ (\blacktriangle) and $\Lambda = 10$ (\bullet). One-photon detunings are $\Delta_A/2\pi = \Delta_B/2\pi = 4$ GHz and all results are obtained with $\tau = 2 \mu\text{s}$. (b) The transfer inefficiency $1 - P_{max}$ corresponding to the values of η_{opt} calculated in (a). The oscillations of the curves are attributed to Rabi dynamics and it should be noted that the curves are symmetric with respect to letting $r \rightarrow r^{-1}$.

III. OPTICAL BLOCH EQUATIONS

The previous section developed analytical criteria for maintaining adiabaticity when Gaussian pulses are used and when the one-photon detunings are much larger than Rabi frequencies. We now turn to numerical simulations of the detection scheme taking into account the full dynamics and using realistic experimental parameters. We solve the optical Bloch equations describing the dynamics of the five levels depicted in Fig. 1, but ignore magnetic sublevels. We stay within the dipole approximation and define the Rabi frequencies

$$\Omega_A = \mu_{12}E_A/\hbar \quad (14)$$

$$\Omega_B = \mu_{32}E_B/\hbar \quad (15)$$

$$\Omega_C = \mu_{34}E_C/\hbar \quad (16)$$

$$\Omega_D = \mu_{54}E_D/\hbar \quad (17)$$

where μ_{ij} are the dipole matrix elements and E_i laser field amplitudes. The laser fields with frequencies ω_{ij} are not necessarily on resonance and we introduce detunings $\Delta_{ij} = \frac{\mathcal{E}_i - \mathcal{E}_j}{\hbar} - \omega_{ij}$ with respect to the atomic energy levels $\{\mathcal{E}_i\}$. With the notation of Fig. 1 we define $\Delta_A = \Delta_{21}, \Delta_B = \Delta_{23}, \Delta_C = \Delta_{43}$ and $\Delta_D = \Delta_{45}$. Furthermore, we apply the rotating wave approximation to arrive at the interaction Hamiltonian for the system

$$H = \sum_{i=1}^5 \hbar \omega_i \rho_{ii} + (\hbar \Omega_A \rho_{12} + \hbar \Omega_B \rho_{32} + \hbar \Omega_C \rho_{34} + \hbar \Omega_D \rho_{54} + h.c.), \quad (18)$$

where $\omega_i = \mathcal{E}_i/\hbar$ and the density operator elements are $\rho_{ij} = |j\rangle\langle i|$. Spontaneous emission is introduced as decay terms in the density matrix elements. We neglect spontaneous decay from the metastable $|3\rangle$ and $|5\rangle$ states because their lifetimes are significantly longer than the simulation time (See lifetimes of the different ion species in appendix). Phase fluctuations of the lasers are introduced as decay of the coherences and ion micromotion as a harmonic modulation of the detunings.

In the simulations we use the specific wavelengths ($\lambda_A = 397$ nm, $\lambda_B = 866$ nm, $\lambda_C = 850$ nm, $\lambda_D = 854$ nm) and spontaneous decay rates ($\Gamma_{21}/2\pi = 21$ MHz, $\Gamma_{23}/2\pi = 1.7$ MHz, $\Gamma_{41}/2\pi = 22$ MHz, $\Gamma_{43}/2\pi = 0.18$ MHz, $\Gamma_{45}/2\pi = 1.6$ MHz) for the $^{40}\text{Ca}^+$ ion, but this apart the calculations are also valid for isotopes of Sr^+ , Ba^+ and Hg^+ with no nuclear spin (See relevant parameters for the most abundant isotopes in appendix). We use Gaussian pulses as defined in Eq. (4) with pulse widths $\tau_i = 2\mu\text{s}$. All other parameters are varied depending on which investigations are made. When there is no argument for a different choice we use Rabi frequencies $\Omega_{i,0}/2\pi = 100$ MHz and detunings $\Delta_i/2\pi = 600$ MHz. The delay between pulses is chosen optimal, which in the simulations presented is either $\Delta t = 1.2\mu\text{s}$ or $\Delta t = 1.3\mu\text{s}$. The theory of Sec. II applies when $|\Omega_{i,0}| \ll |\Delta_i|$, which is the case in the majority of the simulations. In these cases we specify the values of η and Λ to make comparison with Sec. II straightforward. For the parameters mentioned above $\eta = 0.85$ or 0.92 and $\Lambda = 9.3$. All parameters for the simulations are mentioned in the figure captions and hence omitted in the text.

To recapitulate, the detection scheme consists of two STIRAP processes. The first transfers population from $|1\rangle$ to $|3\rangle$ applying the A and B -fields as pump and Stokes field, respectively. The second process between $|3\rangle$ and $|5\rangle$ uses C as the pump field and D as the Stokes field.

We first investigate the effect of pulse delay (Sec. IV A), laser detunings (Sec. IV B), laser linewidth (Sec. IV C), pulse width (Sec. IV D) and residual light (Sec. IV E). All these simulations are performed on the latter transition because this transition is subject to spontaneous decay out of the sub-system and thus has a higher sensitivity to non-adiabaticity. An experimental investigation of this transition can be found in [37].

The first STIRAP stage is more sensitive to ion motion because the two laser fields used have very different wavelengths and the Doppler shift induced by the ion mo-

tion therefore gives a large two-photon detuning. Since this stage is responsible for the internal state selection, it is also important to investigate the effect of laser polarization errors and the resulting depletion of the wrong qubit state. The simulations of ion micromotion (Sec. IV F) and polarization errors (Sec. V) are therefore performed on the first STIRAP transition. The simulations are made with all the population initially in $|1\rangle$ or $|3\rangle$ and we find the transfer efficiency as the final population in $|3\rangle$ or $|5\rangle$ for the first or the second STIRAP stage respectively. We assume that the calculated transfer efficiency is equivalent to the qubit detection efficiency, and we do thereby not focus on signal to noise issues of the fluorescence detection of the non-shelved state $|\uparrow\rangle$.

IV. SIMULATIONS IGNORING ATOMIC SPIN

In this chapter we assume perfect laser polarization and hence ignore irrelevant magnetic sublevels of the ions. As mentioned above, we start out by considering the latter $|3\rangle \rightarrow |4\rangle \rightarrow |5\rangle$ STIRAP process.

A. Effect of pulse delay

The first parameter we investigate is the delay between the two pulses and in Fig. 5 we show the transfer efficiency as a function of η for various peak Rabi frequencies $\Omega_{C,0} = \Omega_{D,0}$. Both laser fields are on resonance. The simulations show that for Rabi frequencies above

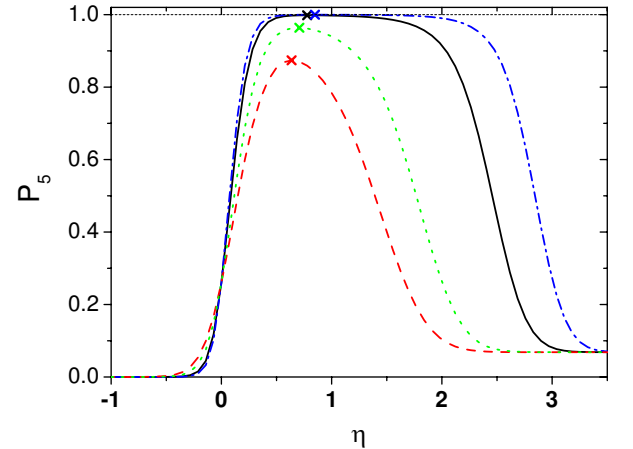


FIG. 5: (Color) Transfer efficiency as a function of delay between pulses for different choices of peak Rabi frequencies: $(- - -)$ $\Omega_{C,0} = \Omega_{D,0} = 2\pi \times 10$ MHz, (\cdots) $\Omega_{C,0} = \Omega_{D,0} = 2\pi \times 20$ MHz, $(—)$ $\Omega_{C,0} = \Omega_{D,0} = 2\pi \times 100$ MHz, $(- \cdot - \cdot)$ $\Omega_{C,0} = \Omega_{D,0} = 2\pi \times 300$ MHz. Positive delay correspond to the counter intuitive pulse sequence, where the laser pulse of field D arrives before the laser pulse of field C . Parameters: $\tau_C = \tau_D = 2\mu\text{s}$ and $\Delta_C = \Delta_D = 0$.

$\Omega_{C,0} = \Omega_{D,0} = 2\pi \times 100$ MHz the transfer efficiency is

close to unity and insensitive to fluctuations in the delay ($P_5 > 0.999$ for fluctuations of η less than 0.2 around the optimal value of 0.85). For smaller Rabi frequencies the transfer efficiency decreases and the sensitivity to delay fluctuations increases. The plateau of $P_5 \simeq 0.07$ for positive η values is the result of optical pumping by the pump field, Ω_C . For $\eta > 0$ this pulse is applied last, and the Stokes field cannot repump population.

We wish to investigate how changes in the delay between pulses influence the transfer efficiency when it is not diminished by other effects. The results of Fig. 5 are therefore calculated for zero one-photon detuning. In this limit the theory of Sec. II is not valid, but in the rest of the work one-photon detunings considerably larger than Rabi frequencies will be used and hence the analytical theory can be used to interpret the numerical simulations.

The results presented in Fig. 5 still show the same trends as the analytical theory. High Rabi frequencies are needed to maintain adiabaticity and, as indicated by the crosses, the delay giving maximum transfer efficiency is found to grow with increasing Rabi frequencies, consistent with Fig. 4.

B. Laser detunings

To reduce the probability of incoherent diabatic excitations we introduce large one-photon detunings of the lasers. Thus, we now investigate the sensitivity of STIRAP to one- and two-photon detunings. The simula-

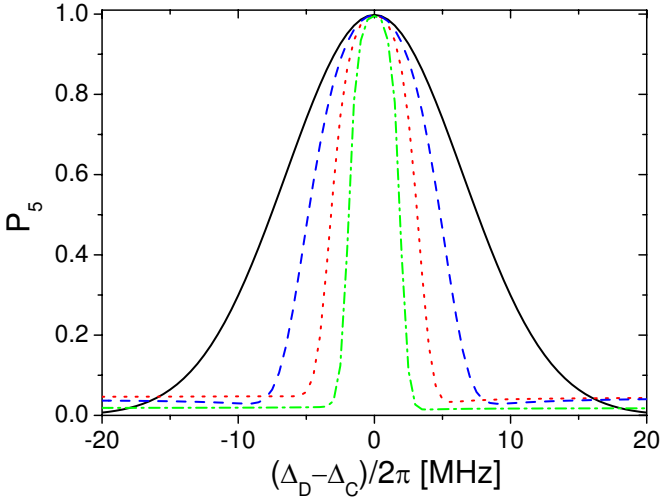


FIG. 6: (Color) Transfer efficiency as a function of two-photon detuning ($\Delta_D - \Delta_C$) of the C and D lasers for different choices of one-photon detuning, Δ_C . The simulations are made with $\Omega_{C,0} = \Omega_{D,0} = 2\pi \times 100$ MHz, $\tau_C = \tau_D = 2 \mu\text{s}$ and $\Delta t = 1.2 \mu\text{s}$ ($\eta = 0.85$). (—) $\Delta_C = 0$ MHz, (---) $\Delta_C = 2\pi \times 300$ MHz ($\Lambda = 18.5$), (····) $\Delta_C = 2\pi \times 600$ MHz ($\Lambda = 9.3$), (-·-·-) $\Delta_C = 2\pi \times 1200$ MHz ($\Lambda = 4.6$).

tions, presented in Fig. 6, show that increasing the one-

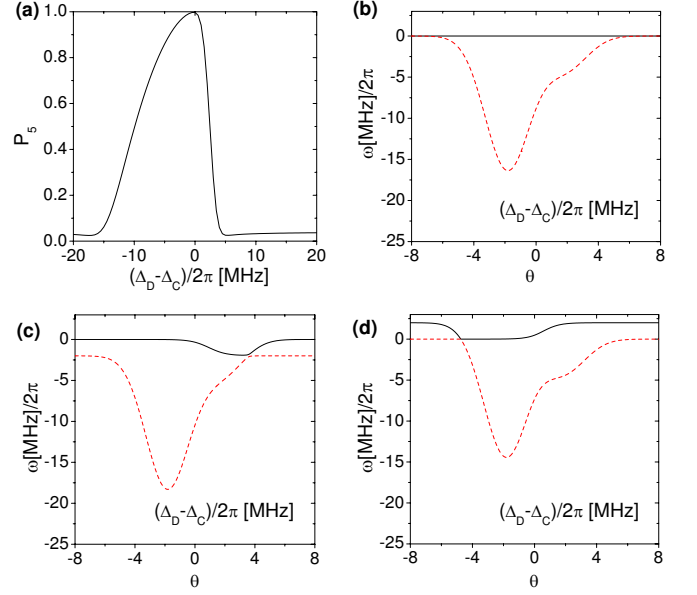


FIG. 7: (Color)(a) Transfer efficiency as a function of two-photon detuning. Evolution of eigenvalues as a function of time is shown in (b): $\Delta_D - \Delta_C = 0$ MHz, (c) $\Delta_D - \Delta_C = 2\pi \times 2$ MHz and (d) $\Delta_D - \Delta_C = -2\pi \times 2$ MHz. In (b), (c) and (d) we use the signatures: (—) ω^D , (---) ω^- . Parameters used for all graphs: $\Omega_{C,0} = 2\pi \times 100$ MHz, $\Omega_{D,0} = 2\pi \times 200$ MHz, $\Delta_C = 2\pi \times 600$ MHz, $\tau_C = \tau_D = 2 \mu\text{s}$ and $\Delta t = 1.2 \mu\text{s}$. ($\Lambda = 18.5$, $\eta = 0.85$).

photon detuning does not limit the transfer efficiency as long as we are close to the two-photon resonance $\Delta_D - \Delta_C = 0$. This criterion gets stricter as we increase the one-photon detuning. If we require $P_5 > 0.99$ the demand on two-photon detuning is $\Delta_D - \Delta_C \pm 2\pi \times 0.5$ MHz when $\Delta_C = 2\pi \times 1200$ MHz as estimated from the dash-dotted curve of Fig. 6. For $\Delta_C = 2\pi \times 600$ MHz, maintaining a two-photon resonance within $2\pi \times 1$ MHz is sufficient as seen from the dotted curve of Fig. 6. An efficient transfer can thus be maintained in spite of a drift from two-photon resonance making STIRAP robust with respect to small frequency drifts of the involved lasers. A closer look at Fig. 6 reveals that the spectra are not exactly symmetric with respect to the sign of the two-photon detuning. With unbalanced Rabi frequencies, $\Omega_{D,0} = 2\Omega_{C,0}$ (See. Fig. 7(a)), the asymmetry becomes more evident. For small negative two-photon detunings the transfer efficiency is much higher than for the corresponding positive two-photon detuning. This effect is due to diabatic transfer between $|d\rangle$ and the energetically closest bright state $|-\rangle$. As discussed in Sec. II this is likely when $|d\rangle$ and $|-\rangle$ are nearly degenerate. The eigenvalues found in Eq. (2) are valid only on two-photon resonance, and the solutions are more complicated in the situation, where this condition is not met. A general expression for the eigenvalues has been derived in [39] and is plotted in Fig. 7(b-d). Here, we show the eigenvalues of $|d\rangle$ (solid curves) and $|-\rangle$ (dashed curves) as a function

of time for three different choices of two-photon detuning. In the case where $\Delta_D - \Delta_C = 0$ MHz (See Fig. 7(b)) the eigenvalues of course coincide when the Rabi frequencies are zero before and after the pulses, but in this case no diabatic transfer will occur as no coupling is present. For positive and negative detunings ($\Delta_D - \Delta_C = 2\pi \times 2$ MHz, Fig. 7(c) and $\Delta_D - \Delta_C = -2\pi \times 2$ MHz, Fig. 7(d)) we see avoided crossings leading to a probability for diabatic transfer to the $|- \rangle$ -state. Such a transfer leads to population of the $|4 \rangle$ -state, which decays rapidly, and the population mainly ends up in $|1 \rangle$. When the energy splitting between the $|d \rangle$ and the $|- \rangle$ state is small, maintaining adiabaticity requires high coupling strengths. For a positive two-photon detuning the avoided crossing occurs late in the sequence, as shown in Fig. 7(c). Here the coupling strength is relatively small due to the asymmetry $\Omega_{D,0} = 2\Omega_{C,0}$, hence the probability of diabatic transfer is large. With a negative two-photon detuning the avoided crossing occurs early, as shown in Fig. 7(c). The coupling is stronger at this time and the probability of diabatic transfer is thus smaller. This difference gives rise to the asymmetry of the two-photon spectrum in Fig. 7(a).

C. Laser linewidths

Laser phase fluctuations lead to dephasing between the three states involved and may therefore affect STIRAP. This dephasing effect has been studied thoroughly in [40], where the STIRAP transfer efficiency has been shown to depend only on the dephasing rate between $|3 \rangle$ and $|5 \rangle$, γ_{35} .

$$P_5 = \frac{1}{3} + \frac{2}{3} e^{-3\gamma_{35}\tau^2/16\Delta t}, \quad (19)$$

for Gaussian pulses within the adiabatic limit, not taking decay from $|4 \rangle$ into account. In Fig. 8 we present simulations showing the exact influence of the laser phase fluctuations parameterized by the laser linewidth. Also shown as the full curve is Eq. (19). The curves show that the transfer efficiency is strongly limited by the laser phase fluctuations and because of the non-zero decay from $|4 \rangle$ the situation is even worse than predicted by Eq. (19). For high Rabi frequencies the coupling is stronger and therefore the limitations due to dephasing are less pronounced. To maintain a transfer efficiency above 0.99 we find laser linewidths required to be below $2\pi \times 1.5$ kHz for $\Omega_{C,0} = \Omega_{D,0} = 2\pi \times 100$ MHz and below $2\pi \times 2$ kHz for $\Omega_{C,0} = \Omega_{D,0} = 2\pi \times 300$ MHz. It should be noted that by laser linewidth we mean the frequency fluctuations averaged over the time duration of the experiment. This is not necessarily the steady state laser linewidth. For pulse sequences of roughly $10 \mu s$ duration, as are employed in our simulations, laser linewidths of a few kHz are not unrealistic for most laser systems.

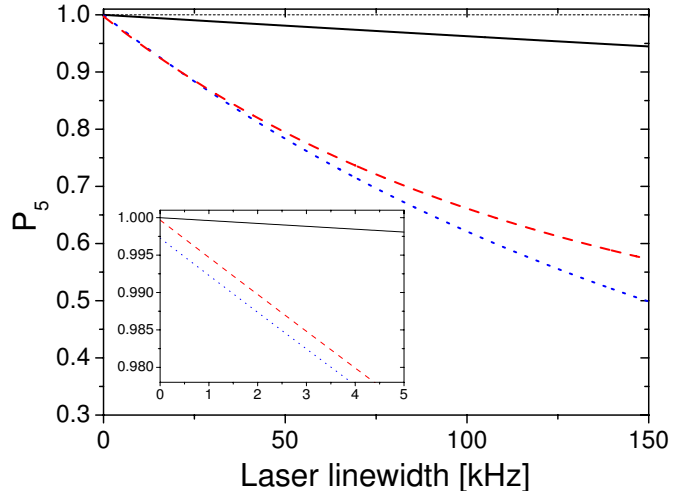


FIG. 8: (Color) Transfer efficiency as a function of the linewidth of the C and D laser fields for different choices of Rabi frequencies. The simulations use $\tau_C = \tau_D = 2 \mu s$, $\Delta t = 1.2 \mu s$ ($\eta = 0.85$) and $\Delta_C = \Delta_D = 2\pi \times 600$ MHz. (—) $P_5 = 1/3 + 2/3 \exp(-3\gamma_{35}\tau^2/16\Delta t)$, (---) $\Omega_{C,0} = \Omega_{D,0} = 2\pi \times 300$ MHz ($\Lambda = 83.3$), (···) $\Omega_{C,0} = \Omega_{D,0} = 2\pi \times 100$ MHz ($\Lambda = 9.3$).

D. Role of pulse widths

As discussed above, the laser phase fluctuations limit the transfer efficiency, making it preferable to use short pulses, since this typically reduces the effective laser linewidth. Short pulses, however, require higher Rabi frequencies to maintain the adiabaticity. In Fig. 9, we show the transfer efficiency as a function of pulse width in the case of no laser linewidth as well as the case of a $2\pi \times 2$ kHz linewidth. As expected, for the case of no linewidth we find an increasing efficiency as we increase the pulse widths because the criterion for adiabaticity is better fulfilled for larger pulse widths as found in (11). We indicate the point where we exceed 0.995 on the graph. When we introduce a $2\pi \times 2$ kHz laser linewidth an optimum pulse width is found as indicated on the graph.

This optimum depends on the Rabi frequencies of the lasers and the dependency is pictured in Fig. 10. In the case of no linewidth, instead of the optimum, we plot the pulse widths required to exceed a 0.995 transfer efficiency. This result is compared to the optimum pulse width, when lasers have $2\pi \times 2$ kHz linewidth. Both curves show that short pulses are preferred as Rabi frequencies grow. However, the mutual dephasing of the lasers involved, results in smaller optimum pulse widths when finite laser linewidths are introduced. For higher Rabi frequencies, the two curves cross, so that shorter pulse widths apparently are preferred for the perfectly coherent lasers. This is a result of the artificial limit 0.995 chosen to define the black curve. We have assumed the laser linewidths to be constant over the range of pulse durations involved. More realistically one would expect the

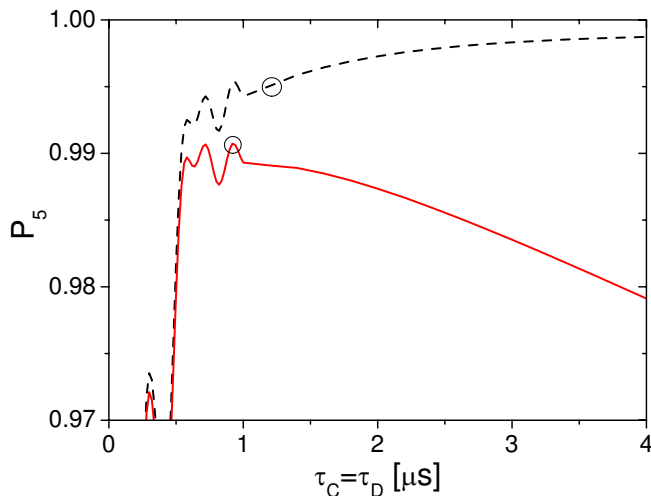


FIG. 9: (Color) Transfer efficiency as a function of pulse width of the C and D laser fields for $2\pi \times 2$ kHz (—) as well as no laser linewidth (---). The delay between the pulses is given by $\eta = 0.85$, laser detunings are $\Delta_C = \Delta_D = 2\pi \times 600$ MHz and peak Rabi frequencies $\Omega_{C,0} = \Omega_{D,0} = 2\pi \times 100$ MHz ($\Lambda = 9.3$).

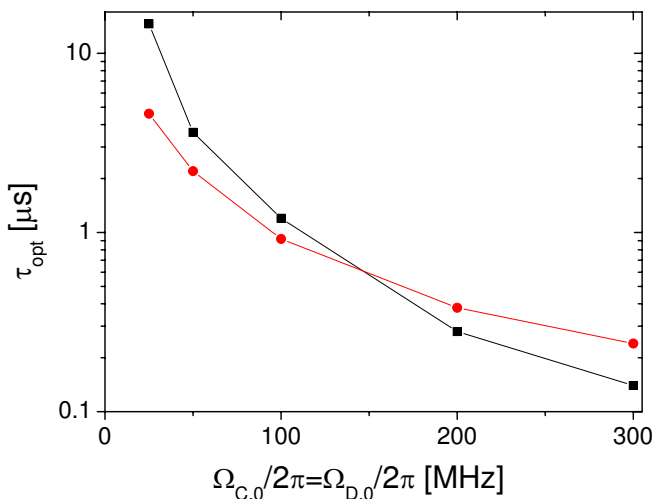


FIG. 10: (Color) Optimal pulse width as a function of the Rabi frequencies of the C and D laser fields for $2\pi \times 2$ kHz (●) as well as no laser linewidth (■). The delay between the pulses is given by $\eta = 0.85$, laser detunings are $\Delta_C = \Delta_D = 2\pi \times 600$ MHz.

laser linewidths to grow proportional to $(\tau_{C,D})^\alpha$, where the power, α , is in the range $0.5 \rightarrow 1$ for a phase diffusion process.

E. Residual light

In the first generation of STIRAP experiments beams of atoms passed through two stationary laser beams [28, 30]. Here, the detection region was spatially well

separated from the STIRAP region and in this case no residual light was present. When we consider the situation with stationary ions and pulsed laser beams, the situation is less favorable. In the case of a constant background level of laser light, the ions do not start out in an exact dark state and hence population transfer may be limited by the resulting finite population of the short lived states $|2\rangle$ and $|4\rangle$. Moreover, since the residual light is able to excite the Raman resonance between the states $|3\rangle$ and $|5\rangle$, repumping of the transferred population can take place after ended STIRAP pulse sequence. With a small background level of light this Raman resonance will be narrow and hence the limitation of population transfer is most severe near two-photon resonance as experimentally found in [37]. Assuming Rabi frequencies of $2\pi \times 100$ MHz and extinction ratio $\approx 10^{-4}$ of the optical pulse generators, we arrive at residual Rabi frequencies in the MHz range, which can easily repump a significant portion of the shelved population on two-photon resonance. In this section we address this problem and establish upper limits on the peak Rabi frequencies involved.

We denote the Rabi frequency of the residual light $\Omega_{\text{off},i}$, $i = \{A, B, C, D\}$. We first look at the transfer efficiency as a function of the two-photon detuning. When no residual light is present the transfer efficiency is optimal on two-photon resonance as shown previously in Fig. 6, but this is no longer the case when we introduce a fraction of residual light, $\Omega_{\text{off},i}/\Omega_{i,0}$. In Fig. 11(a) we present the transfer efficiency as a function of two-photon detuning for different fractions of residual light. As we increase this fraction we see an increasing loss of population on two-photon resonance. With $\Omega_{\text{off},i}/\Omega_{i,0}$ less than 0.02 (dashed curves) this loss is only a few percent relative to the maximum transfer efficiency. However, already with $\Omega_{\text{off},i}/\Omega_{i,0} = 0.05$ (solid curve) the loss has grown to nearly 50 % near two-photon resonance, rendering the detection scheme useless in this case.

As mentioned earlier, residual light is typically present as a fraction of the peak Rabi frequencies, and hence very high Rabi frequencies are not necessarily preferable. In Fig. 11(b) we show the transfer efficiency as a function of the peak Rabi frequencies in the STIRAP pulses for different values of the fraction of residual light. Increasing the Rabi frequencies increases the transfer efficiency until the residual light limits the transfer. The maximum transfer efficiency is found to be 0.99 around the Rabi frequencies, $\Omega_{C,0} = \Omega_{D,0} = 2\pi \times 50$ MHz with a residual light level less than $\Omega_{\text{off},i}/\Omega_{i,0} = 0.02$. For even higher Rabi frequencies we observe Rabi-floppings between $|3\rangle$ and $|5\rangle$.

Experimentally $\Omega_{i,0}/2\pi = 100$ MHz can be achieved focusing a beam with a mW power level to a μm spot size. Switching of the lasers with acousto-optical modulators or electro-optical modulators can be done on ns timescale reducing the power level to a few hundred nW which correspond to $\Omega_{\text{off},i}/\Omega_{i,0} = 0.01$. This is represented by the green dotted curve in Fig. 11(b), which obviously reveals the limitations set by residual light. The extinction ra-

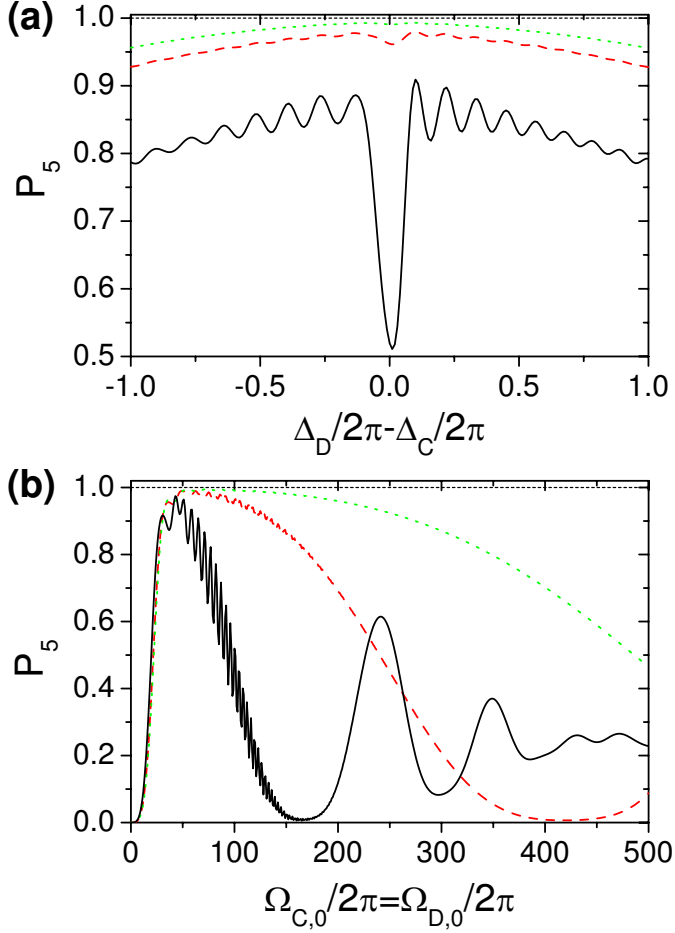


FIG. 11: (Color) (a) Transfer efficiency as a function of two-photon detuning with $\Omega_{C,0} = \Omega_{D,0} = 2\pi \times 100$ MHz and $\Delta_C = 2\pi \times 600$ MHz. $\Lambda = 9.3$. (b) Transfer efficiency as the peak Rabi frequencies are varied, simulated with $\Delta_C = \Delta_D = 2\pi \times 600$ MHz. The different curves represent different fractions of residual light: (\cdots) $\Omega_{\text{off},i}/\Omega_{i,0} = 0.01$, ($- - -$) $\Omega_{\text{off},i}/\Omega_{i,0} = 0.02$ and ($—$) $\Omega_{\text{off},i}/\Omega_{i,0} = 0.05$. Parameters used in simulations: $\tau_C = \tau_D = 2 \mu\text{s}$, $\Delta t = 1.2 \mu\text{s}$, yielding $\eta = 0.85$. The total time duration is $20 \mu\text{s}$ and laser linewidth has been ignored.

tio 10^{-4} correspond to the situation where the lasers are extinguished by one optical pulse generator. Applying additional AOM's and EOM's in succession will reduce the residual light level, and as a result, the limitation due to this light can be smaller as well, at the expense of increased experimental complexity.

F. Ion motion

The ions have so far been considered as having no motion with respect to the laser fields. We consider the ions to be confined in a linear Paul trap [41], where they experience an effective confining potential due to RF- and DC-fields. The ion motion can be derived to consist of a

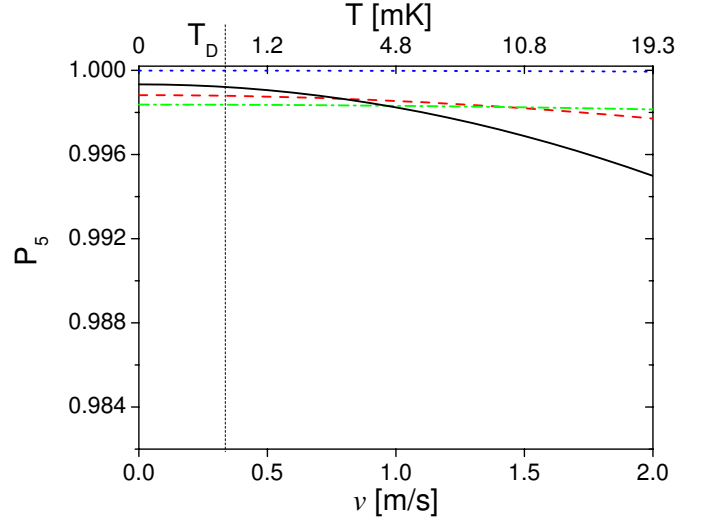


FIG. 12: (Color) Transfer efficiency as a function of the micro-motion velocity. The different curves show results for different detunings: (\cdots) $\Delta_A = \Delta_B = 0$ MHz, ($—$) $\Delta_A = \Delta_B = 2\pi \times 300$ MHz ($\Lambda = 18.5$), ($- - -$) $\Delta_A = \Delta_B = 2\pi \times 600$ MHz ($\Lambda = 9.3$) and ($- \cdot - \cdot -$) $\Delta_A = \Delta_B = 2\pi \times 1200$ MHz ($\Lambda = 4.6$). Parameters used for simulations: $\tau_A = \tau_B = 2 \mu\text{s}$, $\Delta t = 1.3 \mu\text{s}$ ($\eta = 0.92$), $\Omega_A = \Omega_B = 2\pi \times 100$ MHz and $\Omega_{RF} = 2\pi \times 16.8$ MHz. The temperature of the ion is defined as $T = mv^2/k_B$, where m is the ion mass and k_B Boltzmann's constant. The Doppler temperature for Ca^+ , T_D , is indicated by the vertical line.

three-dimensional harmonic motion with frequencies ω_x , ω_y and ω_z called the secular motion [41]. In addition the RF-field drives an oscillation with the RF-frequency, Ω_{RF} . This oscillation is called the ion micromotion. The secular frequencies are typically much smaller than Ω_{RF} and hence STIRAP transfer efficiency is mainly limited by the micromotion. The effect of micromotion is simulated by modulating the detunings as

$$\Delta_i(t) = \Delta_i(0) - v \frac{2\pi}{\lambda_i} \cos(\Omega_{RF}t). \quad (20)$$

We only consider micromotion in one dimension with maximum velocity v . This classical treatment of micromotion is justified by quantum Monte Carlo simulations where the ion motion has been quantized showing no visible difference between classical and quantized motion [42]. Another argument for this classical simplification is the strength of the laser fields making $\Omega_{i,0} \gg \Omega_{RF}$. As discussed previously, the STIRAP transfer efficiency is more sensitive to two-photon than one-photon detunings. If we assume co-propagating laser fields and take the $^{40}\text{Ca}^+$ ion as an example, the two-photon detuning will be strongly modulated in the case of the $|1\rangle$ - $|2\rangle$ - $|3\rangle$ transition where the two laser fields have a large wavelength difference $(\Delta\lambda/\lambda)_{123} = 0.54$, while the $|3\rangle$ - $|4\rangle$ - $|5\rangle$ transition experiences a much smaller modulation of the two-photon detuning $(\Delta\lambda/\lambda)_{345} = 0.005$. This means that the first transition, in the case of $^{40}\text{Ca}^+$, is strongly

limited by micromotion while the second remains virtually unaffected.

In Fig. 12 we show the transfer efficiency as a function of the micromotion velocity for different choices of detuning. The simulations show that when we increase the one-photon detuning the micromotion velocity becomes an increasingly limiting factor. For small micromotion velocities we see that the transfer efficiency is higher for small one-photon detunings. This is due to a decreased sensitivity to a non-vanishing two-photon detuning as discussed in Sec. IV B. For higher velocities the one-photon detuning is strongly modulated. This results in sidebands, of which the high frequency component comes close to resonance, hereby inducing real transitions to the short lived $|2\rangle$ -state. This effect gets more evident when the one-photon detuning is close to $v\frac{2\pi}{\lambda_i}$, which for our parameters varies between 0 and 100 MHz. Fig. 12 shows small sensitivity to micromotion for very small and very large values of $\Delta_A = \Delta_B$, while the $\Delta_A = \Delta_B = 2\pi \times 300$ MHz trace shows a rapid drop as a function of v . For the chosen parameters a micromotion velocity below 1 m/s ensures a transfer efficiency above 0.998. From the kinetic energy of the ion a temperature can be defined through the relation $\frac{1}{2}k_B T = \frac{1}{2}mv^2$. Hence, in the case of $^{40}\text{Ca}^+$ a velocity below 1 m/s correspond to a temperature below 4.8 mK. When the ion is Doppler laser cooled, temperatures below the so-called Doppler temperature, T_D , cannot be obtained. For $^{40}\text{Ca}^+$ $T_D = 0.5$ mK as indicated by the vertical line on Fig. 12. This is well below the required 4.8 mK and Doppler cooling is thus sufficient to achieve a high transfer efficiency. Doppler temperatures for other relevant ions can be found in Table I.

V. POLARIZATION REQUIREMENTS

Until this point Zeeman sublevels have been ignored. However, in order to investigate the effect of laser polarization, deviating from purely circular, we now introduce all of the Zeeman sublevels of the first stage STIRAP. The optical Bloch equations for the full eight level system are derived analogous to the equations in Sec. III. We consider the field A to have both σ_{\pm} polarization components as well as a possible π component in case of magnetic field errors. The second STIRAP field, B , is assumed to have perfect σ_- polarization. We denote the σ_+ polarized component of Ω_A by Ω_A^+ , the σ_- polarized component by Ω_A^- and the π polarized component by Ω_A^0 (See Fig. 13).

Efficient qubit projection requires all population moved from $|\downarrow\rangle$ to the $D_{3/2}$ levels while leaving the $|\uparrow\rangle$ population unchanged. In order to test these criteria we simulate the problem with two different initial states corresponding to all population in $|\downarrow\rangle$ and $|\uparrow\rangle$ respectively. The results are shown in Fig. 14. First we focus on the situation, where all initial population is in the $|\downarrow\rangle$ qubit state. Ideally the final populations in both qubit states

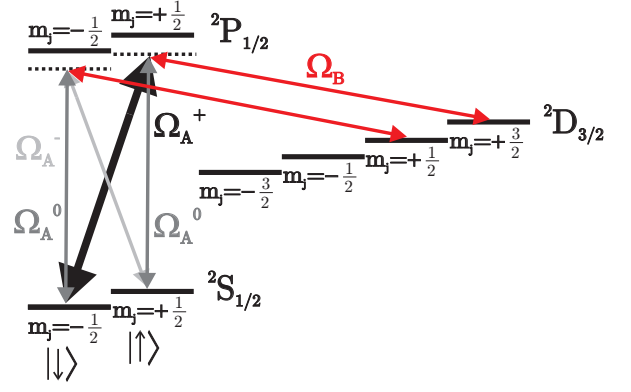


FIG. 13: (Color) Zeeman sublevels of the three states involved in the first STIRAP process. The $S_{1/2}$ and $P_{1/2}$ states are coupled by a laser field with a σ_+ polarized component (Ω_A^+), a σ_- polarized component (Ω_A^-) and a π polarized component (Ω_A^0). The $D_{3/2}$ and $P_{1/2}$ states are coupled by a laser field (Ω_B) with a pure σ_- polarization.

should be vanishing for our scheme to work. The results, shown in Fig. 14 (a) and (b), reveal that detection errors can be kept below 0.01 provided the magnetic field can be controlled accurately enough to keep Ω_A^0/Ω_A^+ below 0.02. However, when all initial population is in the $|\uparrow\rangle$ state, the situation is worse. From Fig. 14 (c), we find that the population in the $|\uparrow\rangle$ state is pumped out as the relative amplitude of the σ_- polarized component is increasing. This is of course undesirable. Hence, in order to keep qubit detection errors below 0.01 for an arbitrary initial state, we must demand that $\Omega_A^0/\Omega_A^+ < 0.02$ and $\Omega_A^-/\Omega_A^+ < 0.04$ with the parameters used in this simulation.

VI. FULL SIMULATION

Finally, we present the results of a simulation of the full two stage STIRAP population transfer including all of the above described effects except polarization errors. The parameters relevant to the simulation can be found in the caption of Fig. 15. The figure shows the population transfer efficiency as a function of the two-photon detuning, $\Delta_B - \Delta_A$, for the first STIRAP stage. Assuming that the ions can be kept cooled close to the Doppler temperature, we have chosen a temperature of 0.8 mK due to the micromotion for this simulation. The resulting peak velocity of 0.4 m/s results in a loss of population transfer of less than 0.01 according to the discussion of Sec. IV F. The two-photon detuning of the second STIRAP stage has been chosen to be zero and the residual power level is chosen to yield a Rabi frequency of 0.01 relative to the peak Rabi frequencies for all four optical fields.

From Fig. 15 we find, when all effects are taken into account, a maximum transfer efficiency of 0.97 for

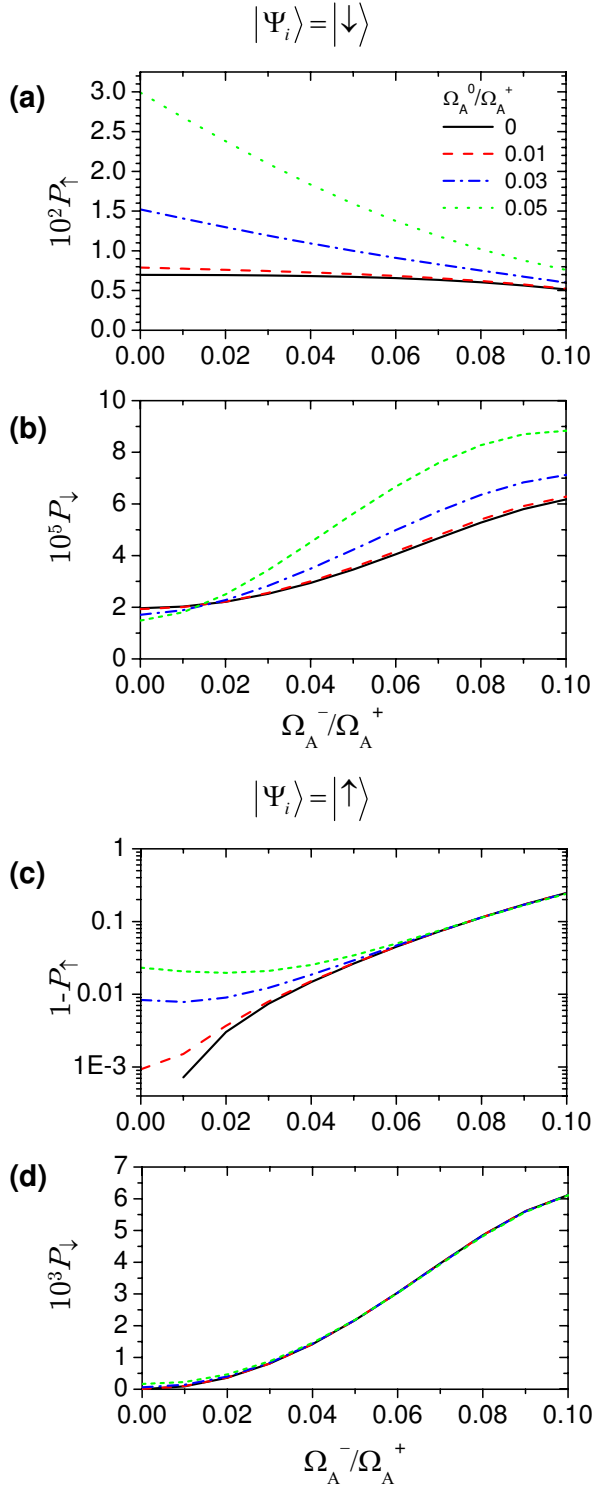


FIG. 14: (Color) Effect of polarization error and error in magnetic field direction. Populations of the qubit states $|\downarrow\rangle$, P_- , and $|\uparrow\rangle$, P_+ , plotted as a function of the relative σ_- polarization component, Ω_A^-/Ω_A^+ . The various curves on each plot correspond to different magnetic field direction errors, parameterized by the relative π polarization component, Ω_A^0/Ω_A^+ . (—) $\Omega_A^0/\Omega_A^+ = 0$, (---) $\Omega_A^0/\Omega_A^+ = 0.01$, (···) $\Omega_A^0/\Omega_A^+ = 0.03$ and (-·-·) $\Omega_A^0/\Omega_A^+ = 0.05$. The upper two graphs, (a) and (b), correspond to all initial population in the $|\downarrow\rangle$ qubit state, while the lower two graphs, (c) and (d), correspond to all initial population in $|\uparrow\rangle$. The parameters for the simulations are $\Omega_{A,0}^+ = \Omega_{B,0} = 2\pi \times 300$ MHz, $\Delta_A = \Delta_B = 2\pi \times 300$ MHz, $\tau = 2$ μ s and $\Delta t = 1.3$ μ s. ($\Lambda = 167$, $\eta = 0.92$).

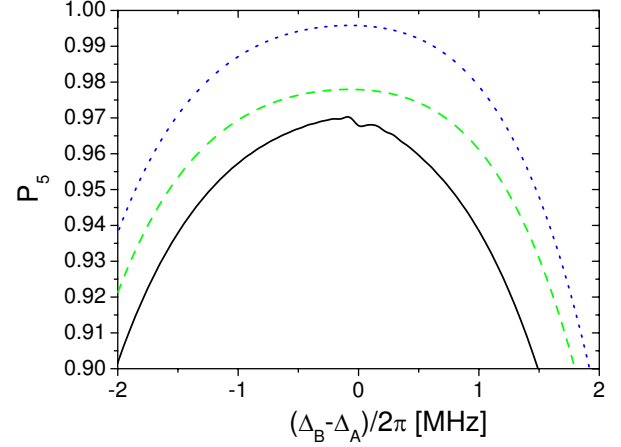


FIG. 15: (Color) Full simulation of the two stage STIRAP. The plot shows the population transfer as a function of two-photon detuning of the first STIRAP stage. Parameters are: $\Delta_A = \Delta_C = \Delta_D = 2\pi \times 600$ MHz, $\Omega_A = \Omega_B = \Omega_C = \Omega_D = 2\pi \times 100$ MHz, $\tau_A = \tau_B = \tau_C = \tau_D = 2$ μ s. All laser linewidths are $2\pi \times 2$ kHz and the trap is characterized by $\Omega_{RF} = 2\pi \times 16.7$ MHz and $v = 0.4$ m/s, corresponding to a temperature of 0.8 mK. The STIRAP's have $\Delta t = 1.2$ μ s corresponding to $\eta = 0.85$ and $\Lambda = 9.3$ for both stages. The two STIRAP stages are separated by 10 μ s and the overall simulation time is 30 μ s. The Rabi frequencies associated with the residual power are 0.01 relative to the peak Rabi frequencies for all four fields. The curves correspond to: (—) all effects on, (---) residual power set to zero but laser linewidth on, and (···) both laser linewidth and residual power set to zero.

$\Delta_B - \Delta_A = -2\pi \times 0.09$ MHz. This corresponds to the full, black curve. In order to identify the processes limiting this efficiency we show with the green, dashed curve the resulting efficiency when the residual optical power is set to zero. Comparison with the full curve shows that a loss in efficiency of almost 0.01 can be attributed to repumping by residual laser light. The blue, dotted curve of Fig. 15 shows the transfer efficiency when both residual light and laser linewidths are set to zero. Here a maximum transfer efficiency of 0.996 is found near two-photon resonance indicating that the finite laser linewidth is indeed a deleterious effect to STIRAP. The linewidth of 2 kHz assigned to all lasers in the simulation results in a loss of transfer efficiency of nearly 0.02. In order to reduce the effect of laser phase fluctuations shorter pulse durations and consequently higher Rabi frequencies must be used.

The simulation illustrates the importance of efficient switching on and off laser power in the STIRAP process. Unless the lasers involved in the two STIRAP stages are pairwise phase locked one obviously needs fairly high intensities of the optical pulses and hence the requirements to the residual laser power become more stringent. However, as can be seen from Fig. 5, it is noted that the scheme is insensitive to *fluctuations* in the laser power as long as the transitions involved are well saturated and adiabaticity is maintained. Experimentally, high Rabi

frequencies can be achieved at the wavelength listed in the appendix, and the complication of phase locking can thus be avoided [37].

VII. SUMMARY AND CONCLUSIONS

In summary, we analyze the scheme where two magnetic sublevels of the $S_{1/2}$ ground state of alkali earth metal ions are considered as qubit states. We have shown that qubit projection can be effectively performed by electronically shelving the population of one magnetic sublevel via a double STIRAP process. Hereby the population is transferred to the metastable $D_{5/2}$ state and remaining population of the other qubit state can be detected by driving the strong Doppler cooling transition of the ions and spatially monitoring the fluorescence. In order to selectively shelf only one qubit state we apply appropriately polarized light in the first STIRAP process.

We have established the formalism describing the system consisting of the 5 energetically lowest levels of the alkali earth metal ions and we model the STIRAP processes using Gaussian shaped pulses from partially phase coherent lasers. Specific simulations have been performed by solving the optical Bloch equations for the $^{40}\text{Ca}^+$ ion. From these simulations we conclude that our scheme is indeed feasible with a projection efficiency exceeding 99 %, provided laser linewidths can be kept below 1.5 kHz over the timescale of the pulse sequence. The short timespan required to avoid decoherence of the lasers makes it necessary to have high Rabi frequencies in the 100's of MHz regime in order to maintain adiabaticity. However, since we are driving strong, dipole allowed transitions, such high Rabi frequencies can be achieved by using moderately focused lasers with 5-10 mW power.

In order to avoid unwanted excitations, we assume all lasers to be detuned roughly 0.5 - 1 GHz from the one-photon resonance. In the limit of this detuning dominating over Rabi frequencies, we have identified the adiabaticity criteria for the ions when Gaussian light pulses are applied. Given an available laser power and hence certain Rabi frequencies, we find an optimum pulse separation depending only on the parameters, Λ and r . Within variations of 20 % we find the optimum pulse separation to be $\tau/\sqrt{2}$, where τ is the $1/e$ full width of the Gaussian pulses.

In contrast to early STIRAP experiments, where atomic beams and stationary laser beams were used, our system involves stationary atoms and laser pulses. Since the detection zone and the STIRAP zone are spatially identical for stationary ions, we have to take into account the finite extinction ratio of the optical pulse generators involved in the experiment. Due to a finite extinction ratio, a fraction of the peak Rabi frequencies of the STIRAP pulses will be present before and after the pulse sequence. As a result, shelved population can be

repumped, and consequently the shelving efficiency reduced. Clearly mechanical shutters will efficiently block laser beams, exposing the ions, but unfortunately such shutters need several tens of microseconds to activate. On the shorter time scale AOM's and EOM's can be employed with extinction ratios around $1 : 10^4$. Hence, we have analyzed the role of residual light at the level of 10^{-2} in Rabi frequency, and this was found to restrict the shelving efficiency severely if the Rabi frequency exceeded $2\pi \times 100$ MHz. In order for the detection scheme to be more efficient, efforts must be made to extinguish the light even further. This could be achieved by introducing more AOM's or EOM's in succession.

Motion in the ion trap is included in the analysis, and found to be unimportant close to the Doppler cooling limit. For calcium ions this is 0.5 mK.

Finally, we have analyzed the effect of impure polarization of light, which could arise from stray birefringence or variations in the direction of an external magnetic field. Solutions to the optical Bloch equations involving magnetic sublevels of the 3 lowest states of the calcium ion show that projection errors can be kept below 0.01 provided the relative Rabi frequencies of the unwanted polarization components can be kept below 0.02-0.04.

A simulation including all effects outlined above, except polarization errors, show the importance of being able to efficiently switch on and off laser power as well as using highly coherent or perhaps phase locked lasers in this qubit detection scheme. Since we assume that the lasers involved in the scheme are only partially coherent, a loss of transfer efficiency of almost 0.02 is found for laser linewidths of 2 kHz over the time of the experiment. Performing the shelving on a shorter timescale will typically reduce the relevant linewidths but also require higher Rabi frequencies and consequently better suppression of residual laser light.

APPENDIX: RELEVANT ION DATA

Table I shows spectroscopic data for some selected ions possessing the level structure and transitions shown in Fig. 1. Listed are wavelengths, λ_i , associated with the fields Ω_i , $i = \{A, B, C, D\}$, decay rates of the short lived states $|2\rangle$ and $|4\rangle$ into the stable and metastable states as well as decay rates of the metastable states into the stable states and the Doppler temperature, T_D . The data is reproduced from Ref. [43].

ACKNOWLEDGMENTS

This work has been supported by the Danish National Research Council and by the Carlsberg Foundation.

TABLE I: Data of relevant ions

Property	$^{40}\text{Ca}^+$	$^{88}\text{Sr}^+$	$^{138}\text{Ba}^+$	$^{202}\text{Hg}^+$
λ_A [nm]	397	422	493	194
λ_B [nm]	866	1092	650	10670
λ_C [nm]	850	1004	585	991
λ_D [nm]	854	1033	614	398
$\Gamma_{21}/2\pi$ [MHz]	21	20	14	69
$\Gamma_{23}/2\pi$ [MHz]	1.7	1.5	5.3	0.05
$\Gamma_{41}/2\pi$ [MHz]	22	23	19	168
$\Gamma_{43}/2\pi$ [MHz]	0.18	0.18	0.76	0.48
$\Gamma_{45}/2\pi$ [MHz]	1.6	1.4	5.9	40
$\Gamma_{31}/2\pi$ [Hz]	0.15	0.40	0.009	1.62
$\Gamma_{51}/2\pi$ [Hz]	0.15	0.46	0.003	7.96
T_D [mK]	0.50	0.49	0.35	1.7

- [1] M. A. Nielsen and I. L. Chuang, *Quantum Computation and Quantum Information* (Cambridge University Press, Cambridge, 2000).
- [2] A. Wallraff, D. I. Schuster, A. Blais, L. Frunzio, J. Majer, M. H. Devoret, S. M. Girvin, and R. J. Schoelkopf, Phys. Rev. Lett. **95** (2005), 060501.
- [3] M. Steffen, M. Ansmann, R. C. Bialczak, N. Katz, E. Lucero, R. McDermott, M. Neeley, E. M. Weig, A. N. Cleland, and J. M. Martinis, Science **313**, 1423 (2006).
- [4] M. Atature, J. Dreiser, A. Badolato, A. Hoge, K. Karrai, and A. Imamoglu, Science **312**, 551 (2006).
- [5] E. Knill, R. Laflamme, and G. J. Milburn, Nature **409**, 46 (2001).
- [6] R. Prevedel, P. Walther, F. Tiefenbacher, P. Bohl, R. Kaltenbaek, T. Jennewein, and A. Zeilinger, Nature **445**, 65 (2007).
- [7] Q. A. Turchette, C. J. Hood, W. Lange, H. Mabuchi, and H. J. Kimble, Phys. Rev. Lett. **75**, 4710 (1995).
- [8] D. Schrader, I. Dotsenko, M. Khudaverdyan, Y. Miroshnychenko, A. Rauschenbeutel, and D. Meschede, Phys. Rev. Lett. **93** (2004), 150501.
- [9] J. Mompert, K. Eckert, W. Ertmer, G. Birkel, and M. Lewenstein, Phys. Rev. Lett. **90** (2003), 147901.
- [10] I. H. Deutsch, G. K. Brennen, and P. S. Jessen, Fortschr. Phys. **48**, 925 (2000).
- [11] D. J. Wineland, M. Barrett, J. Britton, J. Chiaverini, B. DeMarco, W. M. Itano, B. Jelenkovic, C. Langer, D. Leibfried, V. Meyer, et al., Phil. Trans. R. Soc. Lond. A **361**, 1349 (2003).
- [12] C. Monroe, D. M. Meekhof, B. E. King, W. M. Itano, and D. J. Wineland, Phys. Rev. Lett. **75**, 4714 (1995).
- [13] F. Schmidt-Kaler, H. Häffner, M. Riebe, S. Gulde, G. P. T. Lancaster, T. Deuschle, C. Becher, C. F. Roos, J. Eschner, and R. Blatt, Nature **422**, 408 (2003).
- [14] K. R. Brown, R. J. Clark, J. Labaziewicz, P. Richerme, D. R. Leibbrandt, and I. L. Chuang, Phys. Rev. A **75**, 015401 (2007).
- [15] D. L. Moehring, P. Maunz, S. Olmschenk, K. C. Younge, D. N. Matsukevich, L. M. Duan, and C. Monroe, Nature **449**, 68 (2007).
- [16] S. Seidelin, J. Chiaverini, R. Reichle, J. J. Bollinger, D. Leibfried, J. Britton, J. H. Wesenberg, R. B. Blakestad, R. J. Epstein, D. B. Hume, et al., Phys. Rev. Lett. **96**, 253003 (2006).
- [17] P. C. Haljan, K. A. Brickman, L. Deslauriers, P. J. Lee, and C. Monroe, Phys. Rev. Lett. **94**, 153602 (2005).
- [18] H. Häffner, W. Hänsel, C. F. Roos, J. Benhelm, D. Chek-al kar, M. Chwalla, T. Körber, U. D. Rapol, M. Riebe, P. O. Schmidt, et al., Nature **438**, 643 (2005).
- [19] D. Leibfried, E. Knill, S. Seidelin, J. Britton, R. B. Blakestad, J. Chiaverini, D. B. Hume, W. M. Itano, J. D. Jost, C. Langer, et al., Nature **438**, 639 (2005).
- [20] J. Chiaverini, D. Leibfried, T. Schaetz, M. D. Barrett, R. B. Blakestad, J. Britton, W. M. Itano, J. D. Jost, E. Knill, C. Langer, et al., Nature **432**, 602 (2004).
- [21] D. Møller, L. B. Madsen, and K. Mølmer, Phys. Rev. A **75**, 062302 (2007).
- [22] P. Staanum and M. Drewsen, Phys. Rev. A **66** (2002), 040302(R).
- [23] H. Häffner, F. Schmidt-Kaler, W. Hänsel, C. F. Roos, T. Körber, M. Chwalla, M. Riebe, J. Benhelm, U. D. Rapol, C. Becher, et al., Appl. Phys. B **81**, 151 (2005).
- [24] D. Kielpinski, V. Meyer, M. A. Rowe, C. A. Sackett, W. M. Itano, C. Monroe, and D. J. Wineland, Science **291**, 1013 (2001).
- [25] E. Knill, Nature **434**, 39 (2005).
- [26] A. M. Steane, Nature **399**, 124 (1999).
- [27] J. Oreg, F. T. Hioe, and J. H. Eberly, Phys. Rev. A **29**, 690 (1984).
- [28] K. Bergmann, H. Theuer, and B. W. Shore, Rev. Mod. Phys. **70**, 1003 (1998).
- [29] P. Staanum, Ph.D. thesis, University of Aarhus (2004).
- [30] U. Gaubatz, P. Rudecki, S. Schiemann, and K. Bergmann, J. Chem. Phys. **92**, 5363 (1990).
- [31] L. S. Goldner, C. Gerz, R. J. C. Spreeuw, S. L. Rolston, C. I. Westbrook, W. D. Phillips, P. Marte, and P. Zoller, Phys. Rev. Lett. **72**, 997 (1994).
- [32] J. Lawall and M. Prentiss, Phys. Rev. Lett. **72**, 993 (1994).
- [33] M. Weitz, B. C. Young, and S. Chu, Phys. Rev. A **50**, 2438 (1994).
- [34] T. Cubel, B. K. Teo, V. S. Malinovsky, J. R.

- Guest, A. Reinhard, B. Knuffman, P. R. Berman, and G. Raithel, Phys. Rev. A **72**, 023405 (2005).
- [35] B. Broers, H. B. van Linden van den Heuvell, and L. D. Noordam, Phys. Rev. Lett. **69**, 2062 (1992).
- [36] J. Deiglmayr, M. Reetz-Lamour, T. Amthor, S. Westermann, A. L. de Oliveira, and M. Woldemuller, Opt. Commun. **264**, 293 (2006).
- [37] J. L. Sørensen, D. Møller, T. Iversen, J. B. Thomsen, F. Jensen, P. Staantum, D. Voigt, and M. Drewsen, New J. Phys. **8**, 261 (2006).
- [38] B. W. Shore, K. Bergmann, A. Kuhn, S. Schieman, J. Oreg, and J. H. Eberly, Phys. Rev. A **45**, 5297 (1992).
- [39] M. P. Fewell, B. W. Shore, and K. Bergmann, Aust. J. Phys. **50**, 281 (1997).
- [40] P. A. Ivanov, N. V. Vitanov, and K. Bergmann, Phys. Rev. A **70**, 063409 (2004).
- [41] P. Ghosh, *Ion Traps* (Clarendon Press, Oxford, 1995).
- [42] J. Thomsen, *Master thesis*, Department of Physics and Astronomy (University of Aarhus, 2005).
- [43] D. F. V. James, Appl. Phys. B **66**, 181 (1998).